# Enhanced Open-Circuit Voltage in Visible Quantum Dot Photovoltaics by Engineering of Carrier-Collecting Electrodes

Xihua Wang, Ghada I. Koleilat, Armin Fischer, Jiang Tang, Ratan Debnath, Larissa Levina, and Edward H. Sargent*

Department of Electrical and Computer Engineering, University of Toronto, 10 King's College Road, Toronto, Ontario M5S 3G4, Canada

ABSTRACT: Colloidal quantum dots (CQDs) enable multijunction solar cells using a single material programmed using the quantum size effect. Here we report the systematic engineering of 1.6 eV PbS CQD solar cells, optimal as the front cell responsible for visible—wavelength harvesting in tandem photovoltaics. We rationally optimize each of the device's collecting electrodes—the heterointerface with electron-accepting TiO_2 and the deep-work-function hole-collecting MoO_3 for ohmic contact—for maximum efficiency. We report an open-circuit voltage of 0.70 V, the highest observed in a colloidal quantum dot solar cell operating at room temperature. We report an AM1.5 solar power conversion efficiency of 3.5%, the highest observed in >1.5 eV bandgap CQD PV device.

KEYWORDS: colloidal quantum dot, photovoltaics, electron-accepting electrode, hole-collecting electrode, open-circuit voltage
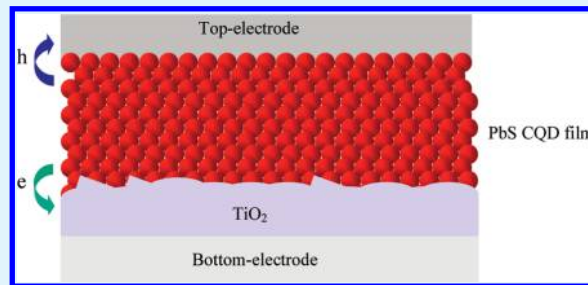
INTRODUCTION

Tuning the bandgap in CQD films is readily achieved via the quantum size effect.[1] Various CQD materials, including CdSe,[2,3] CdS,[4] Cd_3P_2,[5] Si,[6] CIGS,[7] CZTS,[8] PbS,[9,10] and PbSe,[11,12] have exploited tailored spectral response for applications in biological imaging,[13] photodetection,[14] lighting and displays,[15,16] and solar energy harvesting.[17—20]

In photovoltaics (PV), size-effect tuning enables convenient realization of tandem and multijunction solar cells using a single materials processing strategy. In principle, such cells can reach toward higher solar conversion efficiencies than can single-junction cells.[21,22] Recently, a tandem CQD solar cell based on quantum tuning of a single underlying material, PbS, was demonstrated.[23] The optimally chosen front (visible) cell having an ~1.6 eV bandgap was implemented through the use of ~2 nm diameter PbS nanoparticles, whereas the back (infrared) cell was achieved using the same materials tailored to have a 1.0 eV bandgap through the use of 4 nm nanoparticles.

Quantum confinement dominates the exciton energy in 1.6 eV CQD PbS films: this bandgap is fully four times that of the underlying bulk semiconductor (bandgap 0.4 eV). While this dramatic bandgap-tuning is readily achieved at the time of synthesis, it demands, within the photovoltaic device, significant reengineering of the carrier-collecting electrodes to match the altered LUMO and HOMO levels of the light-absorbing quantum dot films. This interface engineering is the subject of the present work.

EXPERIMENTAL SECTION

PbS QD Synthesis and Purification. All chemicals were used as-received unless stated otherwise. Bis(trimethylsilyl)sulphide ($C_6H_{18}S_2Si$; TMS) (0.18 g, 1 mmol) was added to 1-octadecene (ODE) (10 mL), which had been dried and degassed by heating to 80 °C under a vacuum for 24 h. A mixture of oleic acid (1.34 g, 4.8 mmol), oleylamine (0.134 g, 1.5 mmol), PbO (0.45 g, 2.0 mmol), and ODE (14.2 g, 56.2 mmol) was heated to 95 °C under vacuum for 16 h then placed under Ar. The flask temperature was increased to 120 °C and the TMS/ODE mixture was injected. After injection, the temperature dropped to ~95 °C, and the flask was allowed to cool gradually to 36 °C. The nanocrystals were precipitated with 50 mL of distilled acetone and centrifuged. After discarding the supernatant, the precipitate was redispersed in toluene. The nanocrystals were precipitated again with 20 mL of acetone, centrifuged for 5 min, dried, and finally dispersed in toluene (~350 mg/mL). PbS nanocrystals were then refluxed with toluene at 90 °C. The nanocrystals were precipitated two more times with acetone, and finally redispersed in octane at a concentration of 25 mg/mL.

Nanoparticle TiO_2 Electrode Preparation. 10—30 nm TiO_2 nanoparticles originally dispersed in terpineol (DSL90-T, Dyesol) were further diluted in terpineol and spin-coated onto ITO (Delta Technology) substrates. The nanoparticles were diluted with terpineol (1:3 by weight), spin-cast at 1500 rpm, and placed on a hot plate preheated to 120 °C. Substrates were then heated at 200 °C for 15 min and 400 °C for 60 min. Substrates underwent $TiCl_4$ treatment in a 60 mM solution in deionized (DI) water at 70 °C for 30 min. Substrates were removed, rinsed with DI water, and heated at 400 °C for 60 min. The electrode processing was carried out in a fumehood in ambient conditions.

Cyclic-Voltammetry Measurement. We carried out the C-V measurement at room temperature on PalmSens electrochemical station inside a N_2-glovebox, using Ag/AgNO$_3$ (Ag wire within 0.01 M AgNO$_3$ anhydrous acetonitrile solution) as the reference electrode and Pt wire as the counter electrode. Tetrabutylammonium hexafluorophosphate
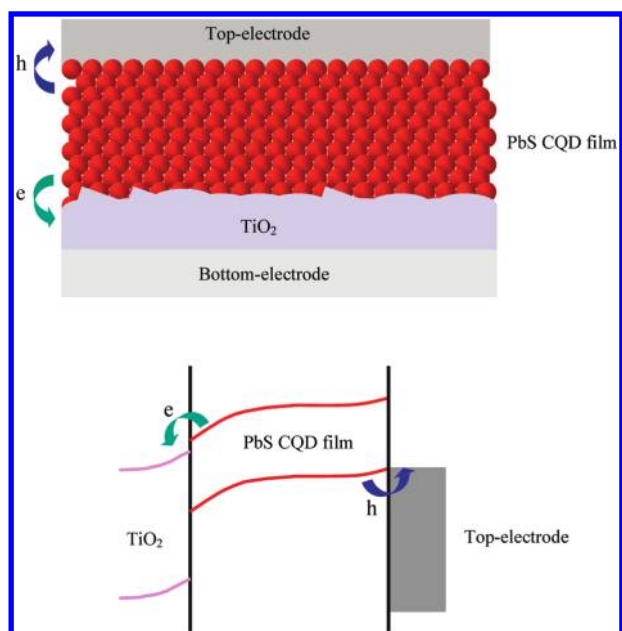
Figure 1. Schematic illustrating in the operation of depleted-heterojunction CQD photovoltaics. The top part of the schematic shows photoexcited carriers being generated and separated inside PbS CQD film. Electrons and holes are depicted as being transported in their respective directions via hopping, following which electrons are injected into the electron-accepting TiO_2, and holes into the top ohmic contact. The bottom part of the schematic shows the spatial band diagram of the device at equilibrium.
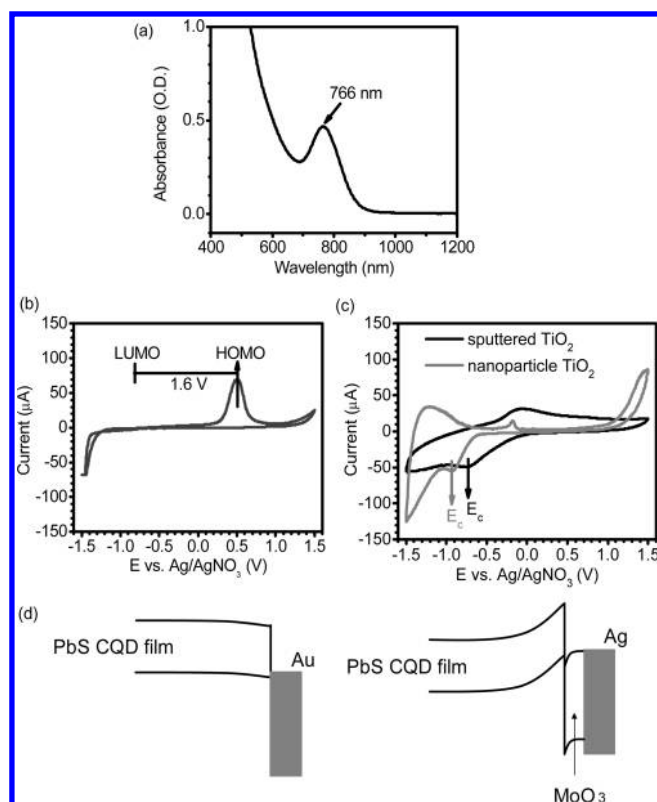

Figure 2. Engineering of electron-accepting materials and hole-collecting top-electrodes. (a) Absorption spectrum of 1.6 eV PbS CQD. (b) Cyclic voltammetry results of PbS CQD film. (c) Cyclic voltammetry results of various electron-collecting TiO_2 films. (d) Schematic of energy band diagram at PbS/top-electrode interface. The PbS/Au contact shows an unfavored band bending of collecting holes. The PbS/MoO_3 contact shows an enhanced band bending via surface-field effect.

(0.1 M) in anhydrous acetonitrile was used as the supporting electrolyte. The scan rate was 0.1 V/s with direction 0 V→ −1.5 V → 0 V→ 1.5 V → 0 V. Using the ferrocene/ferrocenium redox (−4.80 eV relative to vacuum) as the standard reference, we calibrated the Ag/AgNO$_3$ reference electrode as −4.71 eV relative to vacuum.

CQD Deposition. PbS CQDs (1.6 eV) at 25 mg/mL in octane were deposited in a layer-by-layer (LBL) fashion. Two drops of CQDs were dispensed onto the substrates through a 0.2 μm filter and spin-cast at 2500 rpm for 10 s; five drops of a 0.2% mercaptopropionic acid (MPA) in methanol solution were applied to the CQD film through a 0.2 μm filter for 3 s then spin-cast at 2500 rpm. Finally, three rinse steps were carried out: first with methanol, then with acetone, and finally with octane, each followed by spinning the substrate at 2500 rpm for 10 s. This procedure was repeated until the desired film thickness (~200 nm) was reached (12 layers). The device was postsoaked in 10% MPA in methanol for 30 min, and was then rinsed with methanol, acetone, and octane.

Deposition of Sputtered TiO_2 and Top-Electrode Materials. MoO_3 (Alfa Aesar) was deposited by thermal evaporation at a rate of 0.4 Å/s. Ag (Lesker) was deposited by thermal evaporation at a rate of 1 Å/s. The sputterd TiO_2 was sputtered under Ar at 5 mTorr at a rate of 0.2 Å/s. They were deposited using Angstrom Engineering Åmod deposition system in an Innovative Technology glovebox at room temperature. A thermometer monitoring substrate temperature indicated a rise to no greater than 30 °C.

Solar Cell Characterization. Current density−voltage characteristics were measured using a Keithley 2400 source-meter in N_2 ambient. The solar spectrum at AM1.5 was simulated to within Class A specifications (less than 25% spectral mismatch) with a Xe lamp and filters (Solar Light Company Inc.) with measured intensity at 100 mW/cm^2. The source intensity was measured with a Melles-Griot broadband power meter through a circular 0.049 cm^2 aperture at the position of the

device. The accuracy of the power measurement was estimated to be ±5%. The external quantum efficiency spectrum was acquired under 1 sun solar light bias by passing the output of a 400 W Xe lamp through a monochromator and using appropriate order-sorting filters. The resultant monochromatic beam also passed through an optical chopper operating at a frequency of 100 Hz coupled to the input of a Stanford Research Systems lock-in amplifier. The collimated output of the monochromator was measured through a 0.0079 cm^2 aperture with calibrated Newport 818-UV and Newport 818-IR power meters as needed. The measurement step was 20 nm and the intensity varied with the spectrum of the Xe lamp. The monochromatic light was coaligned with an AM 1.5 source (Newport Corporation) providing one-sun intensity of continuous white light bias. The photogenerated current was then measured using a lock-in amplifier.

RESULTS AND DISCUSSION

Depleted-heterojunction colloidal quantum dot photovoltaics[24] have, to date, shown the highest CQD PV device efficiencies. Photogenerated electrons and holes are separated inside a depletion region formed at an n-p interface between n-type TiO_2 and p-type PbS (Figure 1). When suitably designed, the type-II heterojunction with TiO_2 provides a further driving force for electron transfer to the TiO_2 in view of the favorable conduction band offset. Photoholes are collected at a barrierless ohmic contact with the PbS CQD film.

Table 1. PV Device Performance at AM1.5 Illumination; Run-to-Run Variance Is Shown

TiO$_2$ type	PbS CQD	top-electrode	V_{oc} (V)	J_{sc} (mA/cm^2)	FF (%)	PCE (%)
nanoparticle	bandgap 1.6 eV	MoO$_3$	0.70 ± 0.2	9.5 ± 0.5	49 ± 3	3.2 ± 0.3
sputtered	bandgap 1.6 eV	MoO$_3$	0.61 ± 0.1	8.9 ± 0.2	50 ± 2	2.7 ± 0.2
nanoparticle	bandgap 1.6 eV	Au	0.64 ± 0.1	8.1 ± 0.4	49 ± 2	2.6 ± 0.2

The absorption spectrum of PbS CQDs employed herein is shown in Figure 2a. The exciton peak at 766 nm indicates a bandgap of ~1.6 eV. In light of the considerably shallower electron affinity in 1.6 eV PbS CQD films relative to all prior reports (1.3 eV and smaller bandgaps), we first experimentally measured the bandedge of the films, and of various electrodes, using cyclic voltammetry (Figure 2b,c). The calibrated Ag/AgNO$_3$ reference electrode showed an energy of −4.7 eV relative to vacuum. As shown in Figure 2b, the HOMO level was ~5.2 ± 0.1 eV for the quantum dot film, from which we estimate the LUMO level to be at ~3.6 eV ± 0.1. To favor electron injection from the quantum dot film into electron-accepting TiO$_2$, the electron affinity of TiO$_2$ should be deeper than the LUMO level of the quantum dot film. Cyclic voltammetry applied to our TiO$_2$ electrode indicated an electron affinity of ~3.8 eV ± 0.1 eV (Figure 2c). We thus estimated a 0.2 eV energy difference in band offset favoring electron injection into the TiO$_2$. In view of the small (sub 50 meV) exciton binding energy in PbS CQDs, this provided a more than adequate driving force at the heterointerface. Any deeper TiO$_2$ bandedge—such as the −4.0 eV electron affinity reported in sputtered[23] TiO$_2$—would continue to favor electron extraction, but could unduly compromise open-circuit voltage V_{oc} (Table 1).

In general, the lesser of the Femi level difference between electron-collecting and hole-collecting electrodes, and the quasi-Fermi level splitting inside the PbS film, sets the upper limit of open-circuit voltage V_{oc} in heterojunction solar cells. In this work, using nanoparticle TiO$_2$, with its −3.8 eV electron affinity, led to a superior V_{oc} of 0.7 V (Table 1) and 3% solar power conversion efficiency (PCE). Using sputtered TiO$_2$ having an electron affinity of −4.0 eV led to a lower V_{oc} (~0.61 V). Our data suggest that the doping of the two species of TiO$_2$ is similar. We offer one explanation of the fact that the open-circuit improves as the electron affinity offset is decreased, but the full quantitative improvement is not fully translated. The lower-performing device may be limited by the excessive loss of energy due to the unnecessarily large electron affinity difference at the interface, whereas the superior device has entered into the regime of being quasi-Fermi-level-splitting-limited.

When working with larger-bandgap materials, challenges arise in constructing barrier-free ohmic contacts using noble metals. This has been previously encountered in, for example, III−V compound semiconductors when lattice matched large-gap nitrides[25] were first introduced in developing blue LEDs. We show that this problem may be solved by using an ultradeep-work-function transparent conductive oxide. We employed MoO$_3$, a heavily doped deep-work-function metal oxide, to achieve ohmic contact to 1.6 eV PbS CQD film. The thermally evaporated MoO$_3$ was characterized[23] and had a work function of 5.4 eV, and provided direct work-function match to the HOMO level (5.2 eV) of 1.6 eV PbS CQD film. Slight band-bending at PbS/MoO$_3$ interface in fact favors hole collection and achieves a mild back surface field that repels electrons from this interface[26] (Figure 2b). We showed the enhanced PV device performance
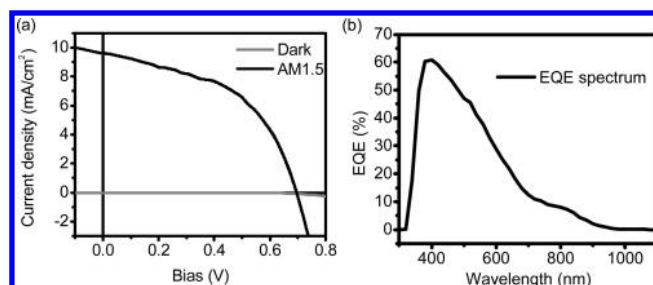

Figure 3. Characterization of PbS CQD based solar cells. (a) AM1.5 $J−V$ characteristics. V_{oc} = 0.70 V, short-circuit current J_{sc} = 10 mA/cm^2, fill factor FF = 50%, PCE = 3.5%; (b) EQE spectrum of the device.

with MoO$_3$ top electrode compared to the commonly employed Au top electrode (Table 1, Au work function 5.1 eV). Attractively, evaporated Ag serve as a highly effective reflective top electrode atop MoO$_3$, obviating the use of Au entirely.

We conclude with more complete characterization of our PV devices behaviors. In Figure 3 we provide current density−voltage ($J−V$) and external quantum efficiency (EQE) spectra for the best PV device achieved through the combination of these optimization strategies reported herein.

CONCLUSION

In summary, we synthesized visible quantum dots (1.6 eV PbS CQD) and applied them to photovoltaic devices with electron-accepting TiO$_2$ and hole-collecting MoO$_3$. We characterized and further customized the electrical properties of the carrier-collecting electrodes. PV devices with an enhanced V_{oc} of 0.70 V are only obtained after engineer carrier-collecting electrodes for both electrons and holes. The 3.5% AM1.5 PCE achieved herein represents the highest power conversion efficiency reported in a visible (~1.6 eV bandgap) quantum dot PV device.

AUTHOR INFORMATION

Corresponding Author
*E-mail: ted.sargent@utoronto.ca.

ACKNOWLEDGMENT

REFERENCES

(1) Rossetti, R.; Nakahara, S.; Brus, L. E. *J. Chem. Phys.* **1983**, *79*, 1086–1088.

(2) Murray, C. B.; Norris, D. J.; Bawendi, M. G. *J. Am. Chem. Soc.* **1993**, *115*, 8706–8715.

(3) Yu, K.; Hu, M. Z.; Wang, R.; Piolet, M. L.; Frotey, M.; Zaman, M. B.; Wu, X.; Leek, D. M.; Tao, Y.; Wilkinson, D.; Li, C. *J. Phys. Chem. C* **2010**, *114*, 3329–3339.

(4) Ma, N.; Yang, J.; Stewart, K. M.; Kelley, S. O. *Langmuir* **2007**, *23*, 12783–12787.

(5) Wang, R.; Ratcliffe, C. I.; Wu, X.; Voznyy, O.; Tao, Y.; Yu, K. *J. Phys. Chem. C* **2009**, *113*, 17979–17982.

(6) Kelly, J. A.; Shukaliak, A. M.; Fleischauer, M. D.; Veinot, J. G. C. *J. Am. Chem. Soc.* **2011**, *133*, 9564–9571.

(7) Panthani, M. G.; Akhavan, V.; Goodfellow, B.; Schmidtke, J. P.; Dunn, L.; Dodabalapur, A.; Barbara, P. F.; Korgel, B. A. *J. Am. Chem. Soc.* **2008**, *130*, 16770–16777.

(8) Guo, Q.; Hillhouse, H. W.; Agrawal, R. *J. Am. Chem. Soc.* **2009**, *131*, 11672–11673.

(9) McDonald, S. A.; Konstantatos, G.; Zhang, S.; Cyr, P. W.; Klem, E. J. D.; Levina, L.; Sargent, E. H. *Nat. Mater.* **2005**, *4*, 138–142.

(10) Fu, H.; Tsang, S.-W.; Zhang, Y.; Ouyang, J.; Lu, J.; Yu, K.; Tao, Y. *Chem. Mater.* **2011**, *23*, 1805–1810.

(11) Law, M.; Luther, J. M.; Song, Q.; Hughes, B. K.; Perkins, C. L.; Nozik, A. J *J. Am. Chem. Soc.* **2008**, *130*, 5974–5985.

(12) Liu, H.; Guyot-Sionnest, P. *J. Chem. Phys. C* **2010**, *114*, 14860–14863.

(13) Resch-Genger, U.; Grabolle, M.; Cavaliere-Jaricot, S.; Nitschke, R.; Nann, T. *Nat. Methods* **2008**, *5*, 763–775.

(14) Konstantatos, G.; Howard, I.; Fischer, A.; Hoogland, S.; Clifford, J.; Klem, E.; Levina, L.; Sargent, E. H. *Nature* **2006**, *442*, 180–183.

(15) Caruge, J. M.; Halpert, J. E.; Wood, V.; Bulovic, V.; Bawendi, M. G. *Nat. Photon.* **2008**, *2*, 247–250.

(16) Tu, C.-C.; Tang, L.; Huang, J.; Voutsas, A.; Lin, L. Y. *Appl. Phys. Lett.* **2011**, *98*, 213102.

(17) Tang, J.; Sargent, E. H. *Adv. Mater.* **2011**, *23*, 12–29.

(18) Pattantyus-Abraham, A. G.; Kramer, I. J.; Barkhouse, A. R.; Wang, X.; Konstantatos, G.; Debnath, R.; Levina, L.; Raabe, I.; Nazeeruddin, M. K.; Grätzel, M.; Sargent, E. H. *ACS Nano* **2010**, *4*, 3374–3380.

(19) Dutta, M.; Basak, D. *J. Nanoparticle Research* 2011, 10.1007/s11051−011−0517−6.

(20) Tsang, S.-W.; Fu, H.; Ouyang, J.; Zhang, Y.; Yu, K.; Lu, J.; Tao, Y. *Appl. Phys. Lett.* **2010**, *96*, 243104.

(21) Sargent, E. H. *Nat. Photon.* **2009**, *3*, 325–331.

(22) Henry, C. H. *J. Appl. Phys.* **1980**, *51*, 4494–4500.

(23) Wang, X.; Koleilat, G. I.; Tang, J.; Liu, H.; Kramer, I. J.; Debnath, R.; Brzozowski, L.; Barkhouse, D. A. R.; Levina, L.; Hoogland, S.; Sargent, E. H. *Nat. Photon.* **2011**, *5*, 480–484.

(24) Liu, H.; Tang, J.; Kramer, I. J.; Debnath, R.; Koleilat, G. I.; Wang, X.; Fisher, A.; Li, R.; Brzozowski, L.; Levina, L.; Sargent, E. H. *Adv. Mater.* **2011**, *23*, 3832–3837.

(25) Nakamura, S.; Mukai, T.; Senoh, M. *Appl. Phys. Lett.* **1994**, *64*, 1687–1689.

(26) von Roos, O. *J. Appl. Phys.* **1978**, *49*, 3503–3511.